energies

MDPI

Article

Mechanical Behavior of Coupled Elastoplastic Damage of Clastic Sandstone of Different Burial Depths

Yu Zhang [1,2,*], Lu Wang [1], Goangseup Zi [1,3] and Yan Zhang [1]

1 College of Pipeline and Civil Engineering, China University of Petroleum, Qingdao 266555, China; wanglultr@163.com (L.W.); g-zi@korea.ac.kr (G.Z.); hypons33@163.com (Y.Z.)
2 Key Laboratory of Deep Earth Science and Engineering (Sichuan University), Ministry of Education, Chengdu 610065, China
3 School of Civil, Environmental & Architectural Engineering, Korea University, Seoul 02841, Korea
* Correspondence: zhangyu@upc.edu.cn; Tel.: +86-1379-283-9259

Received: 4 March 2020; Accepted: 23 March 2020; Published: 2 April 2020

Abstract: Clastic sandstone is widely distributed in oil and gas reservoirs; its internal structure has many micro-defects. Under different stress environments of burial depth, significant damage evolution and plastic deformation easily occur. A series of triaxial compression tests were performed to study the coupled elastoplastic damage mechanical behavior of clastic sandstone samples at different burial depths ranging from 581.28 m to 979.82 m. Results reveal that the stress-strain responses of clastic sandstone samples exhibit significant nonlinear and softening characteristics. The mechanical behavior is due to the coupling of plastic deformation and mechanical damage. Plastic and damage internal variables cause damage stiffness degradation and plastic flow. Considering the coupling of elastoplastic damage in the loading process, an elastoplastic damage coupling model is proposed to study the mechanical behavior of different burial depth clastic sandstones. The model can effectively describe the mechanical behavior of clastic sandstone, such as the volume compression and dilatancy transformation, plastic hardening and damage softening, which are in good agreement with the experimental results. Furthermore, the mechanical behavior of the clastic sandstone shows a dependency on the confining pressure and burial depth. The load-bearing capacity and the ability to resist deformation of the clastic sandstone are improved as the confining pressure and burial depth increase. Relevant results can provide reliable basis for the safe exploitation of oil and gas engineering.

Keywords: clastic sandstone; elastoplastic damage; elastoplastic damage coupling model; burial depth

1. Introduction

The clastic reservoir is the key research target of oilfield exploration and development [1–5]. As source rock is solidified by sand, clay and gypsum, the reservoir clastic rock minerals are microcrystalline, with complex internal structure, a wide distribution of micro-defects and rich organic matter [6–8]. Under the action of deep, high-crustal stress, micro-defects in clastic rock easily expand and propagate. The internal structure is subject to plastic deformation and damage evolution, which leads to the degradation of the mechanical property. Therefore, the strength of the clastic reservoir is evidently reduced, thereby causing casing damage and a large deformation of the reservoir [9–16].

Generally, clastic sandstone contains a considerable number of micro-defects from the effects of sedimentation. Defects cause the mechanical properties of clastic sandstone to become extremely complex. Furthermore, different burial depths lead to changes in mechanical properties. Laboratory tests have been conducted to estimate the effect of burial depth on the physical and

mechanical properties of rock [17–20]. The residual stress and peak deviatoric stress, as well as the corresponding axial strain and volumetric strain, increase with the increase of confining pressure and burial depth. However, the Poisson's ratio increases negatively with the increase of confining pressure; the influence of confining pressure and burial depth on elastic modulus is not significant [21,22]. However, most studies focus on qualitative analysis of experimental results. The modelling of coupled elastoplastic damage mechanical behavior and the change law of mechanical parameters of clastic sandstone under different burial depths have not been effectively identified.

During oil and gas exploration and development, the effect of external construction disturbance causes stress to be concentrated easily on the reservoir, leading to elastoplastic deformation and damage evolution of clastic rocks in the reservoir. The crustal stress of a reservoir increases gradually as the burial depth increases. Thus, the elastoplastic deformation and damage evolution of reservoir clastic rock become more evident; the coupling effect of elastoplastic damage is also significant. However, at present, the study on the response of elastoplastic damage coupling of reservoir clastic rock in different burial depths is unclear. Therefore, a series of triaxial compression tests of reservoir clastic sandstone with different burial depths was conducted to study the mechanical behavior of elastoplastic deformation and damage evolution. Moreover, an elastoplastic damage coupling model is proposed and the effects of different burial depths on the mechanical parameters of clastic sandstone are discussed.

2. Triaxial Compression Test of Different Burial Depths of Clastic Sandstone

2.1. Experimental Material and Procedure

Clastic sandstone samples were drilled from different burial depths of 581.28, 679.39, 780.00, 881.50 and 979.82 m in a gas reservoir site in the northern South China Sea. Considering the sample of clastic sandstone at 979.82 m, the clastic sandstone in this depth range is grey argillaceous siltstone with fine silt and massive structures (Figure 1). The internal structure has defects under the influence of structural stress and other factors. The clastic rock is mainly composed of clastic (43%), interstitial material (50%) and opaque mineral (7%), among which the clastic components are quartz (30%), plagioclase (3%) and biotite (10%); the interstitial materials are calcite (35%), muscovite (5%) and cryptocrystalline (10%). The particle size of the debris is 0.02–0.05 mm; the mineral structure is granular, flaky and tabular; the particle size of the filler is 0.05 mm; the mineral structure is granular, bladed and elongated; the porosity is 0.86%.

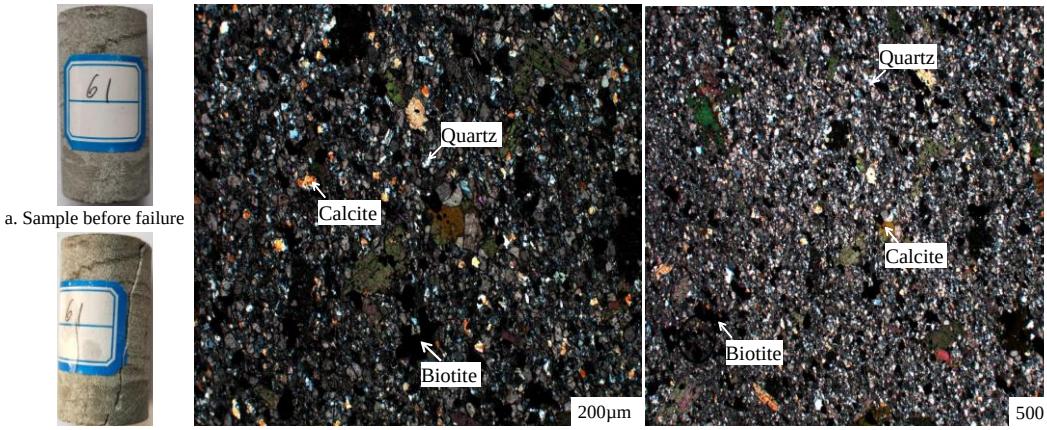

Figure 1. Typical clastic sandstone sample during the triaxial compression test.

All tests were conducted under drained condition using servo-controlled triaxial equipment at room temperature [23,24], as shown in Figure 2. Cylinder samples were used with an average size of 25 mm in diameter and 50 mm in height (Figure 1). Repetitive triaxial compression tests were

performed on the five groups of clastic sandstone samples with different buried depths under different confining pressures, such as 10, 20 and 30 MPa. The confining pressure and axial load were applied at a constant rate of 0.75 MPa/min. The strain during the first stages of confining pressure was neglected in the triaxial tests.

Figure 2. Servo-controlled triaxial equipment during laboratory tests.

2.2. Mechanical Behavior of Triaxial Compression Tests

Figure 3 depicts the typical stress-strain curves for different values of confining pressure and burial depth. Significant nonlinear and softening characteristics can be observed from all sample series. The entire deformation process of the samples consists of an elastic stage, yield stage, plastic hardening stage and damage softening stage.

The clastic sandstone, which is mostly composed of rock materials, exhibits an evident pressure-dependent behavior. During the initial loading, a quasi-linear stress-strain relation is obtained, which is reversible. This finding represents the elastic compressibility of the rock skeleton. In this phase, the elastic bulk modulus can be obtained according to the slope of the stress-strain curve. When the stress reaches yield stress, the deformation of the material enters a nonlinear plastic stage. At this stage, the strain increases significantly and the stress-strain curve is convex. At all confining pressures, non-linear axial deformation begins at an axial strain of approximately 0.5%. With the increase in deviatoric stress, a generally strain-hardening phase is obtained. In this phase, the initiation and propagation of cracks result in strain increase in an unstable manner until peak stress and brittle failure state are attained. Then, in a post-peak softening phase, the deviatoric stress decreases and the internal structure of the sample is highly disrupted.

Moreover, the results showed that the confining pressure and burial depth had significant influence on material response (see Figure 4). Generally, the increase in burial depth and confining pressure is helpful to the closure of the internal micro-defects, thereby improving the load-bearing capacity of the sample. The peak stress increases with the increase in confining pressure and burial depth. The elastic modulus also shows an increasing trend with increasing confining pressure and burial depth. Poisson's ratio varies with confining pressure and burial depth. However, their variations are small and the use of constant values remains reasonable when modelling the plastic behavior and damage evolution is mainly considered.

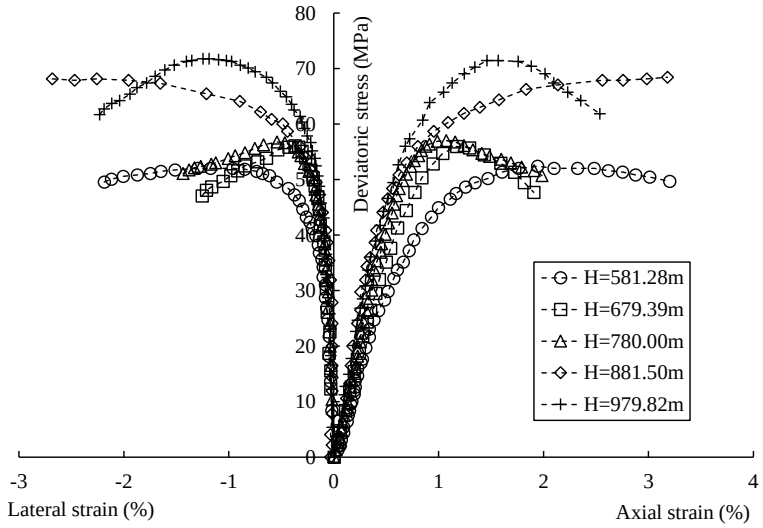

(**a**) Confining pressure: 10 MPa

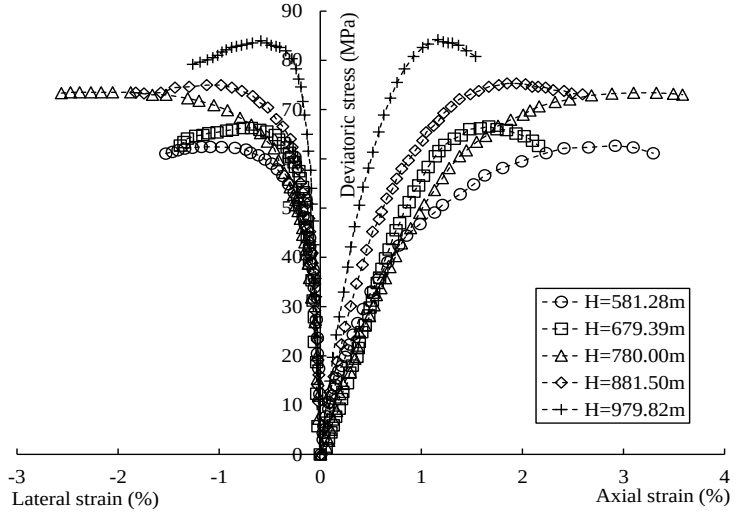

(**b**) Confining pressure: 20 MPa

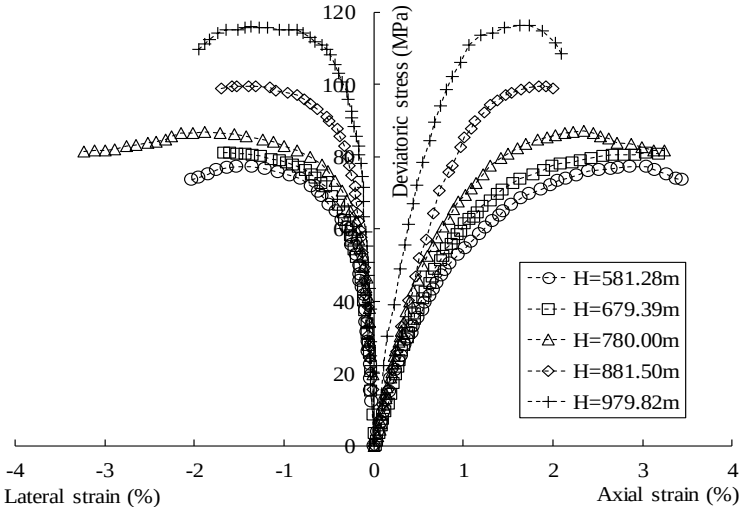

(**c**) Confining pressure: 30 MPa

Figure 3. Stress-strain curves of clastic sandstone at different burial depths in triaxial compression tests.

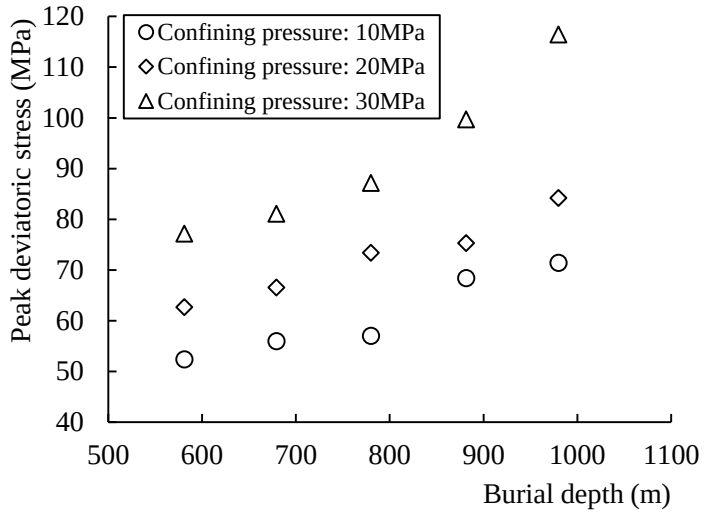

(**a**) Effect of confining pressures and burial depths on the deviatoric stress

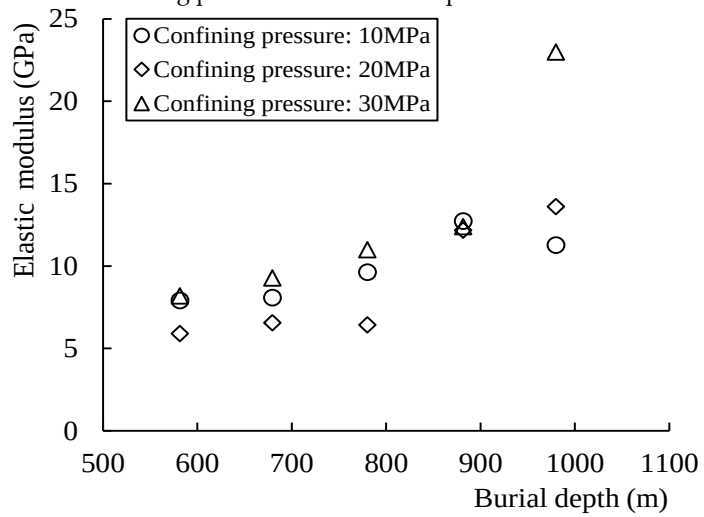

(**b**) Effect of confining pressures and burial depths on the elastic modulus

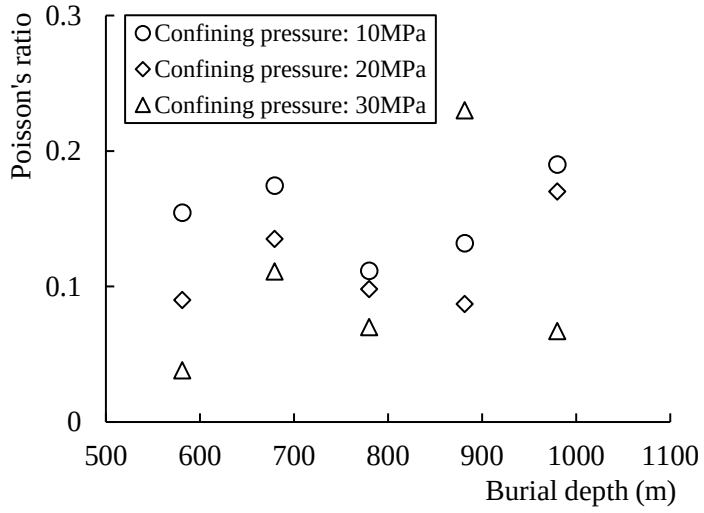

(**c**) Effect of confining pressures and burial depths on the Poisson's ratio

Figure 4. Effect of confining pressures and burial depths on the material response

2.3. Behavior of Volumetric Strain

The failure of clastic sandstone is accompanied by large deformation and volume expansion. The samples showed the transformation from volumetric compressibility to dilatancy in the tests. Volumetric strain (ε_V) can be calculated according to the following formula:

$$\varepsilon_V = \Delta V / V_0 = \varepsilon_1 + 2\varepsilon_3 \quad (1)$$

where ε_1 and ε_3 represent the axial and lateral strain respectively. Considering the samples with a buried depth of 979.82 m, the lateral strain is relatively small at the initial loading stage. In the process of elastic deformation, only the compressible strain is obtained. In this stage, the volumetric strain increases with deviatoric stress. As the deviatoric stress continues to increase, the lateral expansion gradually dominates, resulting in volumetric dilatancy. Moreover, the deformation of the material is inelastic and the volumetric strain increases rapidly. In addition, the increase in confining pressure and burial depth effectively limits the volumetric dilation strain and decreases the maximum volume of compressive strain (see Figure 5).

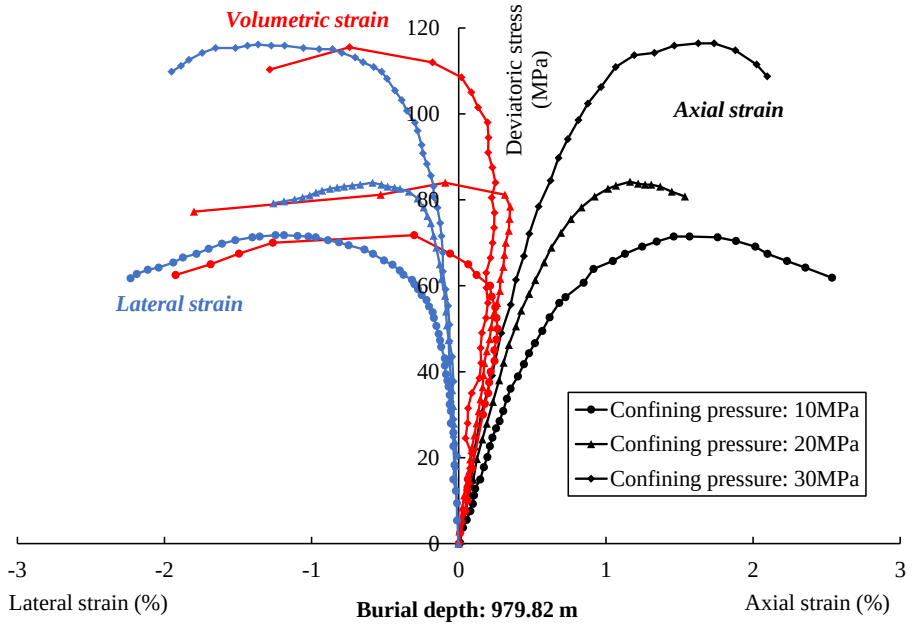

Figure 5. Typical stress-strain curves at different confining pressures in triaxial compression tests.

During the loading process, the volumetric change is closely related to the evolution of internal damage, which is induced by the propagation and coalescence of the micro-defects. At the initial stage of loading, the original micro-defects in the sample gradually closed, resulting in volume compression. At this stage, no new damage is considered. With the increase in deviatoric stress, the volume dilates as the micro-defects grow and the internal damage develops. The corresponding deviatoric stress of volume that reverses from compression to dilatation of clastic sandstone samples is more than 50 MPa. In the failure stage, the sample volume dilates rapidly until the large strain is obtained due to the coalescence of cracks.

2.4. Damage Evolution during Triaxial Compression Tests

The damage evolution caused by the propagation and coalescence of the micro-defects can lead to the degradation of the mechanical behavior of clastic sandstone. The damage variable is used to quantitatively describe the degradation of the rock, which can be calculated in accordance with the stress-strain curve (see Figure 6). On the basis of the inflexion E-point after the peak stress, the damage

variable calculation is divided into two components: (i) the damage variable in I-point is obtained prior to the inflexion E-point:

$$\varepsilon_e^I = \frac{\sigma^I}{E} \tag{2}$$

$$d^I = 1 - \frac{\varepsilon_e^I}{\varepsilon^I} \tag{3}$$

where d is the damage variable, ε is the total strain, ε_e is the elastic strain, σ is the axial stress and E is the elastic modulus and is obtained based on the OF.

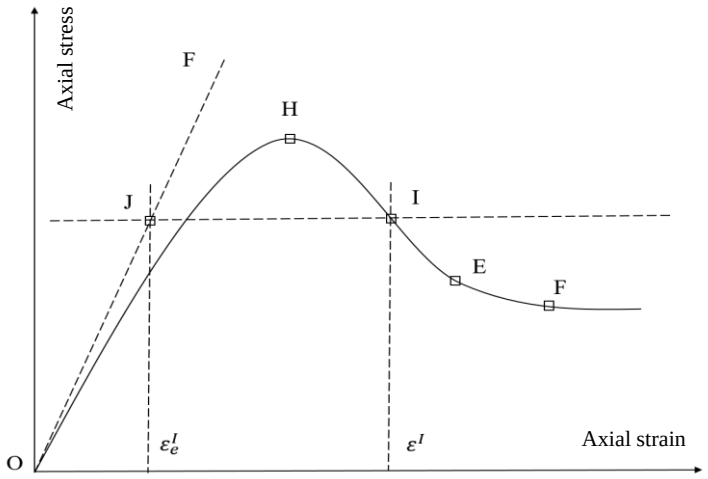

Figure 6. Schematic diagram of damage variable calculation.

(ii) The damage variable in F-point is obtained after the inflexion E-point:

$$d^F = d^E + (1 - \frac{\sigma^F}{\sigma^E}) \tag{4}$$

Therefore, considering the samples with a buried depth of 979.82 m, the damage evolution of clastic sandstone samples under different confining pressures is obtained (see Figure 7). (i) In the elastic stage (OA), the damage of clastic sandstone is very limited; (ii) in the plastic stage (AB), the damage occurs and accumulates rapidly due to the generation and propagation of the micro-defects; (ii) in the post-peak stage (BC), the damage continues to accumulate with the propagation and coalescence of the micro-defects, and the deviatoric stress gradually decreases.

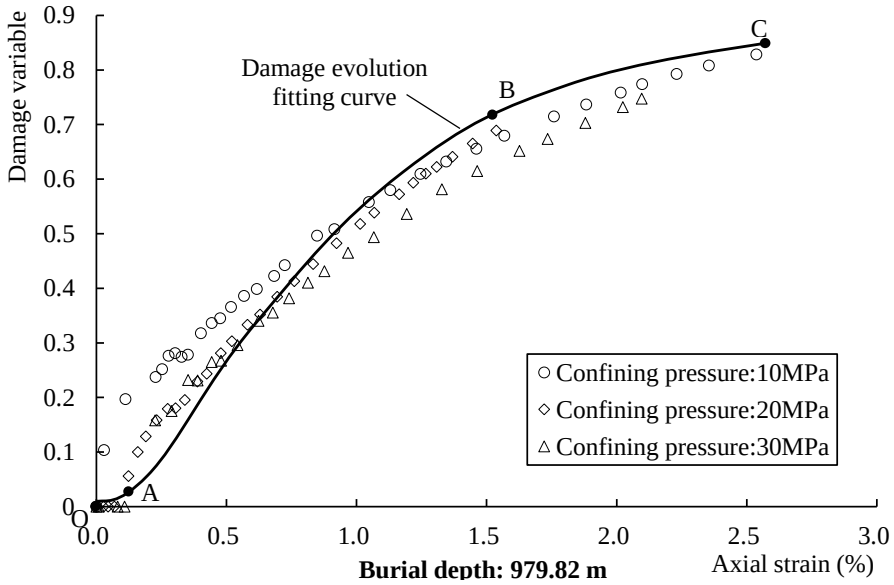

Figure 7. Damage evolution of clastic sandstone under different confining pressures.

3. Elastoplastic Damage Coupling Model

According to the test results, the mechanical response of clastic sandstone is affected by both plastic deformation and damage. Under the assumption of small strains, an elastoplastic damage coupling model needs to be built to describe the mechanical behavior of clastic sandstone. An isotropic scalar damage variable is used to approximate the degradation process caused by the micro-defects.

3.1. Framework of Elastoplastic Damage Coupling Model

Under isothermal condition, the total strain can be divided into elastic strain and plastic strain and the formula is as follows:

$$\boldsymbol{\varepsilon} = \boldsymbol{\varepsilon}^e + \boldsymbol{\varepsilon}^p,\ \mathrm{d}\boldsymbol{\varepsilon} = \mathrm{d}\boldsymbol{\varepsilon}^e + \mathrm{d}\boldsymbol{\varepsilon}^p \tag{5}$$

where $\boldsymbol{\varepsilon}$ is the total strain tensor; $\boldsymbol{\varepsilon}^e$ is the elastic strain tensor; $\boldsymbol{\varepsilon}^p$ is the plastic strain tensor.

The thermodynamic potential of the damaged elastoplastic material is assumed to exist and the damage process is coupled with plastic deformation. The thermodynamic potential is expressed as follows [25]:

$$\psi = \tfrac{1}{2}(\boldsymbol{\varepsilon} - \boldsymbol{\varepsilon}^p) : \boldsymbol{C}(d) : (\boldsymbol{\varepsilon} - \boldsymbol{\varepsilon}^p) + \psi_p(\gamma_p, d) \tag{6}$$

where the symbol ":" represents the two-point product of two tensors; $\boldsymbol{C}(d)$ is the elastic stiffness tensor of damaged material; and the function ψ_p is the thermodynamic potential describing the plastic hardening of clastic sandstone, which can be obtained in accordance with the relationship between hardening function and the thermodynamic potential:

$$\alpha_p = -\partial\psi/\partial\gamma_p = -\partial\psi_p/\partial\gamma_p \tag{7}$$

where γ_p is the internal hardening variable. The constitutive equation is obtained by derivative of thermodynamic potential:

$$\boldsymbol{\sigma} = \frac{\partial\psi}{\partial\boldsymbol{\varepsilon}^e} = \boldsymbol{C}(d) : (\boldsymbol{\varepsilon} - \boldsymbol{\varepsilon}^p) \tag{8}$$

The thermodynamic force is given by the following:

$$Y_d = -\frac{\partial\psi}{\partial d} = -\frac{1}{2}(\boldsymbol{\varepsilon} - \boldsymbol{\varepsilon}^p) : \boldsymbol{C}'(d) : (\boldsymbol{\varepsilon} - \boldsymbol{\varepsilon}^p) - \frac{\partial\psi_p(\gamma_p, d)}{\partial d} \tag{9}$$

The fourth-order tensor $\boldsymbol{C}^{'}(d)$ is obtained by deriving the damage variable from the elastic stiffness tensor:

$$\boldsymbol{C}^{'}(d) = \frac{\partial \boldsymbol{C}(d)}{\partial d} \tag{10}$$

Due to the nonnegativity of internal dissipation, the following inequality is established:

$$\boldsymbol{\sigma} : \dot{\boldsymbol{\varepsilon}}^{p} + Y_d \dot{d} \geq 0 \tag{11}$$

Finally, the incremental form of the constitutive equation (Equation (8)) is obtained:

$$\dot{\boldsymbol{\sigma}} = \boldsymbol{C}(d) : (\dot{\boldsymbol{\varepsilon}} - \dot{\boldsymbol{\varepsilon}}^{p}) + \boldsymbol{C}^{'}(d) : (\boldsymbol{\varepsilon} - \boldsymbol{\varepsilon}^{p})\dot{d} \tag{12}$$

where the dot represents the derivative of a variable over time. The detailed formula of Equation (12) needs to determine the derivative form of damage variable and plastic strain.

3.2. Formulation of Elastoplastic Damage Coupling Model

The behavior of clastic sandstone exhibits high-pressure sensitivity. Under the assumption of small strains, considering the non-linearity in the stress-strain response and the plastic hardening process from the initial plastic yield to the final material failure of clastic sandstone (see Figure 8), the following plastic yield surface equation is adopted:

$$\begin{cases} f = q^2 + A_0 \alpha_p (p - C_0) m_0 = 0 \\ p = -\frac{\sigma_{kk}}{3} \\ q = \sqrt{3J_2} \\ J_2 = \frac{1}{2} s_{ij} s_{ij},\ s_{ij} = \sigma_{ij} - \frac{\sigma_{kk}}{3} \delta_{ij} \end{cases} \tag{13}$$

where A_0 denotes the frictional angle; C_0 denotes the initial cohesion; α_p is the plastic hardening function; p and q are the mean stress and deviatoric stress respectively; m_0 is a constant coefficient used to dimensionalize A_0, which is usually taken as 1 MPa; s_{ij} is the deviatoric stress tensor.

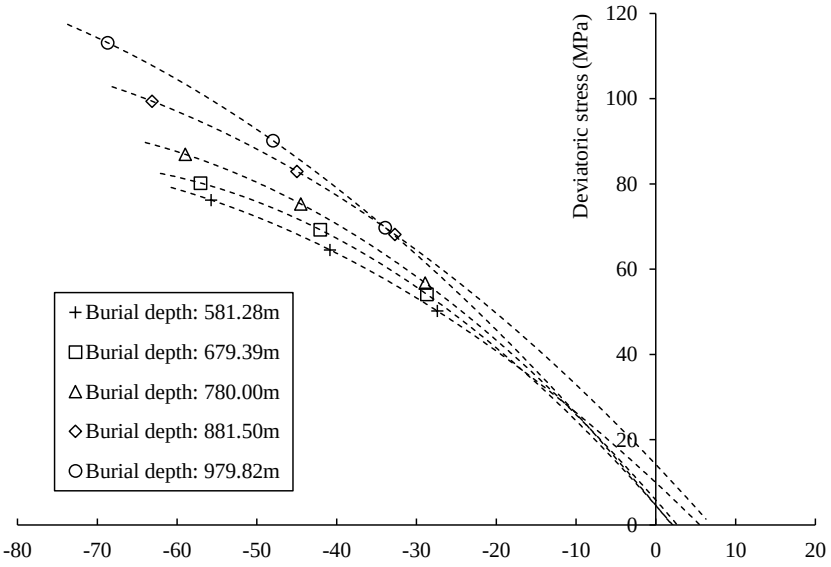

Figure 8. Ultimate yield states of different burial depths clastic sandstones described by mean stress and deviator stress.

In addition, the clastic sandstone has the mechanical behavior of plastic hardening and post-peak softening. The damage is assumed to be isotropic and expressed as a scalar variable d. Moreover,

it is assumed that the strain softening is only related to the damage evolution. Therefore, the plastic hardening behavior is affected by two opposite trends, that is, the hardening function increases with the increase of plastic shear strain γ_p before the peak stress, indicating hardening behavior; after the peak stress, it decreases with the increase of damage variable d, indicating softening behavior [26].

$$\begin{cases} \alpha_p = (1-d)\left[\alpha_p^0 + \left(1-\alpha_p^0\right)\frac{\gamma_p}{b+\gamma_p}\right] \\ \gamma_p = \int \sqrt{\frac{2}{3}\mathrm{d}e_{ij}^p \mathrm{d}e_{ij}^p} \\ e_{ij}^p = \varepsilon_{ij}^p - \frac{1}{3}tr(\boldsymbol{e}^p)\delta_{ij} \end{cases} \tag{14}$$

where α_p^0 is the initial value of the plastic hardening function α_p; b is the plastic hardening parameter; e_{ij}^p is the deviatoric strain tensor; $\mathrm{d}e_{ij}^p$ is the increment of the plastic deviatoric strain tensor; $tr(\boldsymbol{e}^p)$ is the trace of plastic strain tensor.

Furthermore, the plastic strain increment and the plastic flow rule are determined by the plastic potential function. Therefore, a non-associated flow rule is suitable for describing the volumetric compressibility and dilatancy. The plastic potential function is taken as the following form:

$$g = q + A_0(1-d)\eta(p-C_0)\ln\left(\frac{p-C_0}{I_0}\right) = 0 \tag{15}$$

where $I_0 < 0$ denotes the stress state at the intersection of the plastic potential plane and the mean stress axis; η is the parameter that describes the volume compression and dilation.

In the framework of thermodynamics, the damage is generated and expanded under the driving force of the damage. The damage evolution law is determined by a damage criterion, which is a function of damage force [27]:

$$f_d\left(Y_d^p, d\right) = d_c \tanh\left(B_d Y_d^p\right) - d \le 0 \tag{16}$$

where d_c is the final value of damage variable d. The value range of the damage variable is [0, 1]. The parameter B_d controls the dynamic characteristics of damage evolution. Y_d^p is the generalized thermodynamic force related to damage.

In accordance with the relationship between hardening function α_p and thermodynamic potential, the function ψ_p can be expressed by the following:

$$\psi_p = -(1-d)\gamma_p + b(1-d)\left(1-\alpha_p^0\right)\ln\frac{b+\gamma_p}{b} \tag{17}$$

The damage force Y_d^p can be written as follows:

$$\begin{aligned} Y_d^p &= -\frac{\partial\psi}{\partial d} = -\frac{1}{2}(\boldsymbol{\varepsilon}-\boldsymbol{\varepsilon}^p) : \boldsymbol{C}'(d) : (\boldsymbol{\varepsilon}-\boldsymbol{\varepsilon}^p) - \frac{\partial\psi_p(\gamma_p,d)}{\partial d} \\ &= -\frac{1}{2}(\boldsymbol{\varepsilon}-\boldsymbol{\varepsilon}^p) : \boldsymbol{C}'(d) : (\boldsymbol{\varepsilon}-\boldsymbol{\varepsilon}^p) - \gamma_p + b\left(1-\alpha_p^0\right)\ln\frac{\gamma_p+b}{b} \end{aligned} \tag{18}$$

Considering the coupled effect of the plastic behavior and damage evolution, the plastic multiplier $\mathrm{d}\lambda$ and the derivative of the damage variable $\dot{d} = \mathrm{d}d$ can be obtained by solving the plastic consistency condition (Equation (19)) and damage criterion (Equation (20)).

$$\mathrm{d}f = \frac{\partial f}{\partial\boldsymbol{\sigma}}\mathrm{d}\boldsymbol{\sigma} + \frac{\partial f}{\partial d}\mathrm{d}d + \frac{\partial f}{\partial\alpha_p}\frac{\partial\alpha_p}{\partial\gamma_p}\mathrm{d}\gamma_p = 0 \tag{19}$$

$$\begin{cases} \mathrm{d}f_d = \frac{\partial f_d}{\partial d}\mathrm{d}d + \frac{\partial f_d}{\partial Y_d^p}\left(\frac{\partial Y_d^p}{\partial\boldsymbol{\varepsilon}^e}\mathrm{d}\boldsymbol{\varepsilon}^e + \frac{\partial Y_d^p}{\partial\gamma_p}\mathrm{d}\gamma_p\right) = 0 \\ \mathrm{d}\boldsymbol{\varepsilon}^e = \mathrm{d}\boldsymbol{\varepsilon} - \mathrm{d}\lambda\frac{\partial g}{\partial\boldsymbol{\sigma}} \end{cases} \tag{20}$$

3.3. Verification of Elastoplastic Damage Coupling Model

Nine parameters of the model can be obtained from the experimental results. The elastic parameters (E and ν) can be obtained from the linear component of the stress-strain curve. The plastic parameters (C_0 and A_0) can be determined by the intercept and slope of the ultimate yield surface. The initial value of the hardening function α_p^0 is extracted from the relationship between the mean stress and deviatoric stress at the onset of inelastic strain. The plastic hardening parameter b can be calculated according to the relationship between the hardening function and plastic shear strain. The parameter η can be obtained according to the stress state of the transformation point from volumetric compression to dilation. The parameter d_c can be obtained from the residual strength and peak strength of the sample. The parameter B_d can be estimated by fitting the damage evolution curves. The values of model parameters are shown in Table 1.

Table 1. Parameters of the constitutive model.

Burial Depth/m	E/GPa	ν	A_0	C_0/MPa	α_p^0	b	η	B_d	d_c
581.28	7.34	0.094	88.17	11.915	0.0039	0.002	−0.013		
679.39	7.98	0.140	94.39	12.736	0.0054	0.001	−0.014		
780.00	8.74	0.093	138.10	4.020	0.0055	0.003	−0.009	0.75	0.9
881.50	11.66	0.150	80.31	60.471	0.0052	0.005	−0.012		
979.82	15.91	0.142	139.38	28.439	0.0023	0.005	−0.007		

Figure 9 shows the comparisons between the numerical simulations and experimental. In general, the proposed model can accurately describe the mechanical behavior of clastic sandstone, such as plastic behavior, damage evolution and volume transformation from compression to dilation. Furthermore, the coupled behavior of plasticity and damage of post-peak deformation can be effectively described. In addition, the effect of depth on model parameters is mainly concentrated on the parameters of plastic failure criteria (C_0 and A_0), thereby showing an increase in trend with the increase in depth (see Figure 10). Generally, with the increase in burial depth, the micro-defects decrease and the porosity is reduced, thereby increasing its strength.

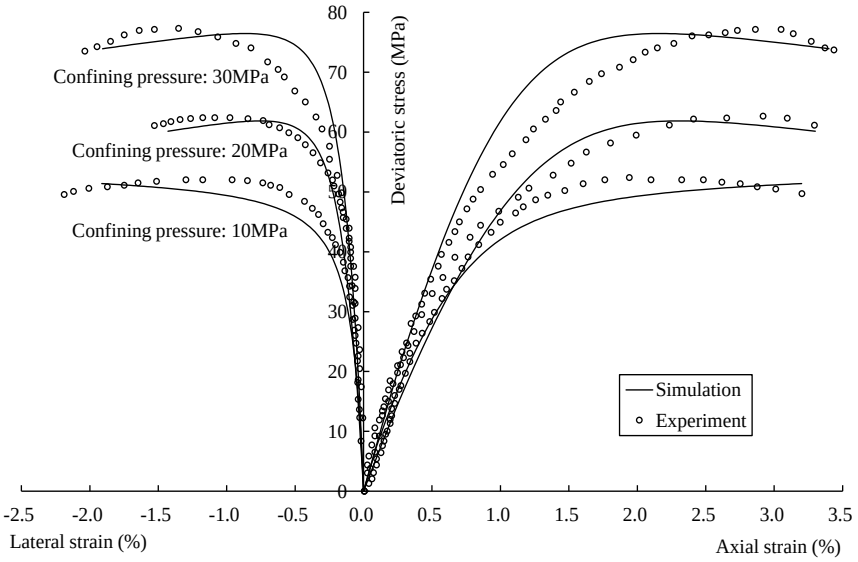

(**a**) Burial depth: 581.28 m

Figure 9. *Cont.*

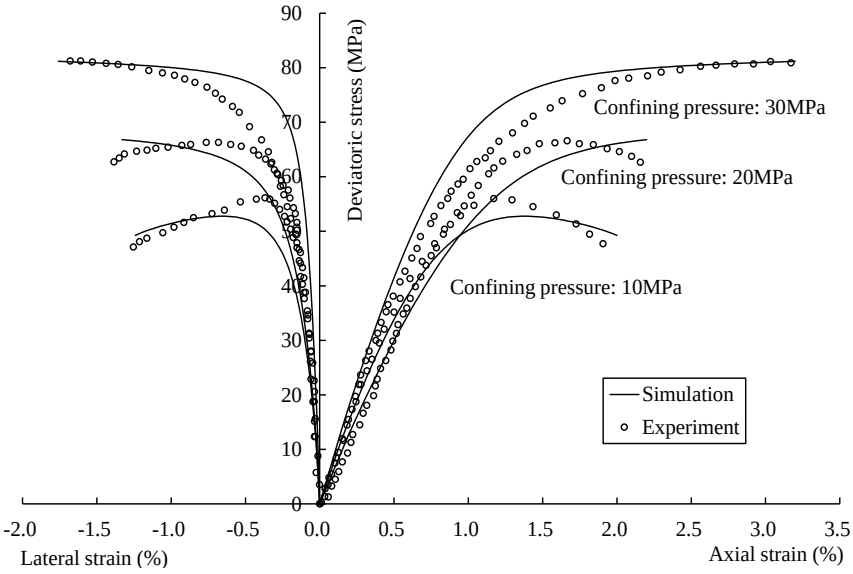

(**b**) Burial depth: 679.39 m

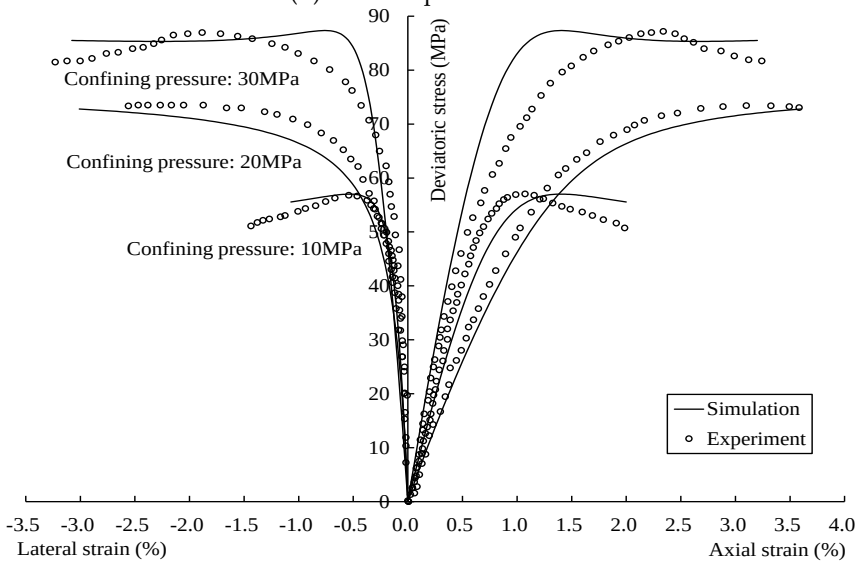

(**c**) Burial depth: 780.00 m

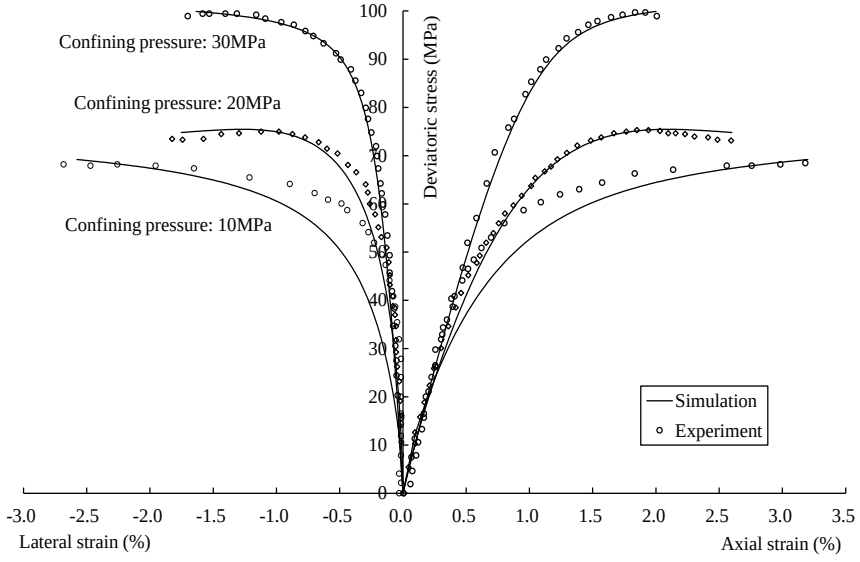

(**d**) Burial depth: 881.50 m

Figure 9. *Cont.*

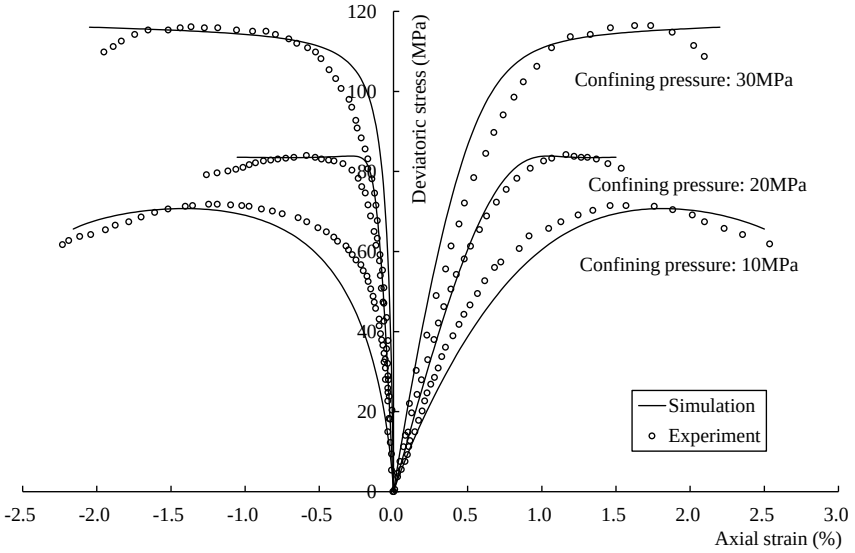

(**e**) Burial depth: 979.82 m

Figure 9. Simulation of triaxial compression tests of clastic sandstone under various confining pressures.

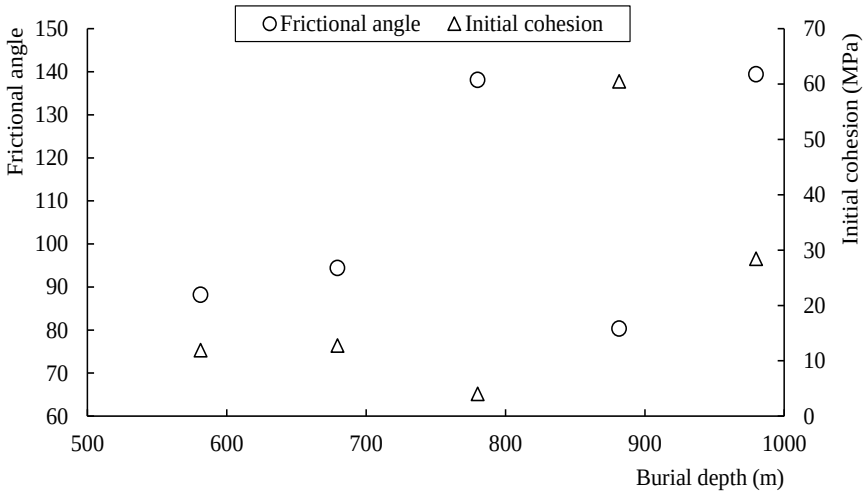

Figure 10. Relationships between the parameters of the model and burial depth.

4. Conclusions

In this paper, the mechanical properties of clastic sandstone under different burial depth were studied by triaxial compression test. The influence of confining pressure and burial depth on rock response was studied. Based on the test results, an elastoplastic damage coupling model was proposed to simulate the mechanical behavior of the samples under different confining pressures and depths. Hence, the following concluding remarks were formulated:

1. The clastic sandstone exhibited an evident pressure-dependent behavior. The entire deformation process of the samples consists of elastic, yield, plastic hardening and damage softening stages. The samples displayed evident volumetric compressibility changes to dilatancy in the tests. It is closely related to the evolution of internal damage which is induced by the propagation and coalescence of the micro-defects.
2. The mechanical response of samples is affected by plastic deformation and damage. A damage variable is used to quantitatively describe the degradation of the rock; the damage evolution of clastic sandstone samples under different confining pressures can be divided into three stages. Thus, an elastoplastic damage coupling model was proposed. This model describes the main

properties of clastic sandstone, such as elastoplastic behavior, the coupling between plastic flow and damage and volume transformation, from compression to dilation.

3. Increasing burial depth and confining pressure can improve the load-bearing capacity and resistance to deformation of the sample. The peak stress and elastic modulus show an increasing trend with increasing confining pressure and burial depth due to the closure of the internal micro-defects in the sample. In addition, the increase in confining pressure and burial depth effectively limits the volumetric dilation strain and decreases the maximum volume of compressive strain.

Author Contributions: Conceptualization, Y.Z. (Yu Zhang); methodology, L.W. and Y.Z. (Yu Zhang); software, L.W.; validation, L.W.; formal analysis, L.W. and Y.Z. (Yan Zhang); investigation, Y.Z. (Yan Zhang); resources, Y.Z. (Yu Zhang); data curation, L.W. and Y.Z. (Yan Zhang); writing—original draft preparation, L.W.; writing—review and editing, Y.Z. (Yu Zhang) and G.Z.; visualization, Y.Z. (Yu Zhang), Y.Z. (Yan Zhang) and L.W.; supervision, Y.Z. (Yu Zhang); project administration, Y.Z. (Yu Zhang); funding acquisition, Y.Z. (Yu Zhang). All authors have read and agreed to the published version of the manuscript.

Funding: Financial support provided by The China Natural Science Foundation (No. 51890914), The Natural Science Foundation of Shandong Province (No. ZR2019MEE001) and The Opening Foundation of Key Laboratory of Deep Earth Science and Engineering (Sichuan University) (DESE201903) is gratefully acknowledged. The authors wish to thank the two reviewers and the editor for their kind advice, which has significantly enhanced the soundness of this paper.

Conflicts of Interest: The authors declare no conflict of interest.

References

1. Zhao, Z.; Du, J.; Zou, C.; Hu, S. Geological exploration theory for large oil and gas provinces and its significance. *Pet. Explor. Dev.* **2011**, *38*, 513–522. [CrossRef]
2. El-Din, E.S.; Mesbah, M.A.; Kassab, M.A.; Mohamed, I.F.; Cheadle, B.A.; Teama, M.A. Assessment of petrophysical parameters of clastics using well logs: The Upper Miocene in El-Wastani gas field, onshore Nile Delta, Egypt. *Pet. Explor. Dev.* **2013**, *40*, 488–494. [CrossRef]
3. Sun, L.; Fang, C.; Sa, L.; Yang, P.; Sun, Z. Innovation and prospect of geophysical technology in the exploration of deep oil and gas. *Pet. Explor. Dev.* **2015**, *42*, 454–465. [CrossRef]
4. Li, M.; Wu, G.; Xia, B.; Huang, T.; Ni, B.; Pang, S.; Long, X. Controls on hydrocarbon accumulation in clastic reservoirs of the Tarim Craton, NW China. *Mar. Pet. Geol.* **2019**, *104*, 423–437. [CrossRef]
5. Monsees, A.C.; Busch, B.; Schöner, N.; Hilgers, C. Rock typing of diagenetically induced heterogeneities—A case study from a deeply-buried clastic Rotliegend reservoir of the Northern German Basin. *Mar. Pet. Geol.* **2020**, *113*, 104163. [CrossRef]
6. Virolle, M.; Brigaud, B.; Luby, S.; Portier, E.; Féniès, H.; Bourillot, R.; Patrier, P.; Beaufort, D. Influence of sedimentation and detrital clay grain coats on chloritized sandstone reservoir qualities: Insights from comparisons between ancient tidal heterolithic sandstones and a modern estuarine system. *Mar. Pet. Geol.* **2019**, *107*, 163–184. [CrossRef]
7. Yang, T.; Cao, Y.; Wang, Y.; Liu, K.; He, C.; Zhang, S. Determining permeability cut-off values for net pay study of a low-permeability clastic reservoir: A case study of the Dongying Sag, eastern China. *J. Pet. Sci. Eng.* **2019**, *178*, 262–271. [CrossRef]
8. Yuan, W. Water-sensitive characterization and its controlling factors in clastic reservoir: A case study of Jurassic the Formation in Northern tectonic zone of Kuqa depression. *Pet. Res.* **2019**, *5*, 77–82. [CrossRef]
9. Salari, M.R.; Saeb, S.; Willam, K.J.; Patchet, S.J.; Carrasco, R.C. A coupled elastoplastic damage model for geomaterials. *Comput. Methods Appl. Mech. Eng.* **2004**, *193*, 2625–2643. [CrossRef]
10. Zhou, J.; Xu, W.; Yang, X. A microcrack damage model for brittle rocks under uniaxial compression. *Mech. Res. Commun.* **2010**, *37*, 399–405. [CrossRef]
11. Shojaei, A.; Taleghani, A.D.; Li, G. A continuum damage failure model for hydraulic fracturing of porous rocks. *Int. J. Plast.* **2014**, *59*, 199–212. [CrossRef]
12. Zhang, Y.; Liu, Z.; Xu, W.; Shao, J. Change in the permeability of clastic rock during multi-loading triaxial compressive creep tests. *Geotech. Lett.* **2015**, *5*, 167–172. [CrossRef]

13. Ma, J.; Zhao, G.; Khalili, N. An elastoplastic damage model for fractured porous media. *Mech. Mater.* **2016**, *100*, 41–54. [CrossRef]
14. Shen, W.; Shao, J. Some micromechanical models of elastoplastic behaviors of porous geomaterials. *J. Rock. Mech. Geotech. Eng.* **2017**, *9*, 1–17. [CrossRef]
15. Zhu, Y. A micromechanics-based damage constitutive model of porous rocks. *Int. J. Rock Mech. Min. Sci.* **2017**, *91*, 1–6. [CrossRef]
16. Bennett, K.C.; Borja, R.I. Hyper-elastoplastic/damage modeling of rock with application to porous limestone. *Int. J. Solids Struct.* **2018**, *143*, 218–231. [CrossRef]
17. Jiang, X.; Wan, L.; Wang, X.; Liang, S.; Hu, B. Estimation of fracture normal stiffness using a transmissivity-depth correlation. *Int. J. Rock Mech. Min. Sci.* **2009**, *46*, 51–58. [CrossRef]
18. Øyvind, M.; Maast, T.E.; Mondol, N.H.; Jahren, J.; Bjørlykke, K. Changes in physical properties of a reservoir sandstone as a function of burial depth-The Etive Formation, northern North Sea. *Mar. Pet. Geol.* **2010**, *27*, 1725–1735.
19. Aschwanden, L.; Diamond, L.W.; Adams, A. Effects of progressive burial on matrix porosity and permeability of dolostones in the foreland basin of the Alpine Orogen, Switzerland. *Mar. Pet. Geol.* **2019**, *100*, 148–164. [CrossRef]
20. Peng, K.; Liu, Z.; Zou, Q.; Wu, Q.; Zhou, J. Mechanical property of granite from different buried depths under uniaxial compression and dynamic impact: An energy-based investigation. *Powder Technol.* **2020**, *362*, 729–744. [CrossRef]
21. Jiang, G.; Zuo, J.; Li, Y.; Wei, X. Experimental investigation on mechanical and acoustic parameters of different depth shale under the effect of confining pressure. *Rock Mech. Rock Eng.* **2019**, *52*, 4273–4286. [CrossRef]
22. Peng, K.; Liu, Z.; Zou, Q.; Zhang, Z.; Zhou, J. Static and dynamic mechanical properties of granite from various burial depths. *Rock Mech. Rock Eng.* **2019**, *52*, 3545–3566.
23. Zhang, Y.; Shao, J.; Xu, W.; Zhao, H.; Wang, W. Experimental and numerical investigations on strength and deformation behavior of cataclastic sandstone. *Rock Mech. Rock Eng.* **2015**, *48*, 1083–1096. [CrossRef]
24. Zhang, Y.; Shao, J.; Xu, W.; Jia, Y. Time-dependent behavior of cataclastic rocks in a multi-loading triaxial creep test. *Rock Mech. Rock Eng.* **2016**, *49*, 3793–3803. [CrossRef]
25. Mohamad-Hussein, A.; Shao, J. Modelling of elastoplastic behavior with non-local damage in concrete under compression. *Comput. Struct.* **2007**, *85*, 1757–1768. [CrossRef]
26. Liu, L.; Xu, W.; Zhao, L.; Zhu, Q.; Wang, R. An experimental and numerical investigation of the mechanical behavior of granite gneiss under compression. *Rock Mech. Rock Eng.* **2017**, *50*, 499–506. [CrossRef]
27. Chen, L.; Shao, J.; Huang, H. Coupled elastoplastic damage modeling of anisotropic rocks. *Comput. Geotech.* **2010**, *37*, 187–194. [CrossRef]